

Ignition and deflagration-to-detonation transition modes in ethylene/air mixtures behind a reflected shock

Cite as: Phys. Fluids **34**, 086105 (2022); <https://doi.org/10.1063/5.0103013>

Submitted: 14 June 2022 • Accepted: 18 July 2022 • Accepted Manuscript Online: 18 July 2022 • Published Online: 09 August 2022

 Zhiwei Huang (黄志伟) and  Huangwei Zhang (张黄伟)



View Online



Export Citation



CrossMark

ARTICLES YOU MAY BE INTERESTED IN

[Predicting the lifetimes of evaporating droplets in ordered arrays](#)

Physics of Fluids **34**, 082010 (2022); <https://doi.org/10.1063/5.0105243>

[Flow Completion Network: Inferring the Fluid Dynamics from Incomplete Flow Information using Graph Neural Networks](#)

Physics of Fluids (2022); <https://doi.org/10.1063/5.0097688>

[On the kinetics of chemical reactions at the detonation of organic high explosives](#)

Physics of Fluids (2022); <https://doi.org/10.1063/5.0095053>

APL Machine Learning

Open, quality research for the networking communities

Now Open for Submissions

LEARN MORE



Ignition and deflagration-to-detonation transition modes in ethylene/air mixtures behind a reflected shock

Cite as: Phys. Fluids **34**, 086105 (2022); doi: [10.1063/5.0103013](https://doi.org/10.1063/5.0103013)

Submitted: 14 June 2022 · Accepted: 18 July 2022 ·

Published Online: 9 August 2022



View Online



Export Citation



CrossMark

Zhiwei Huang (黄志伟),¹  and Huangwei Zhang (张黄伟)^{2,a)} 

AFFILIATIONS

¹School of Aeronautics and Astronautics, Shanghai Jiao Tong University, Shanghai 200240, China

²Department of Mechanical Engineering, National University of Singapore, 9 Engineering Drive 1, Singapore 117576, Singapore

^{a)} Author to whom correspondence should be addressed: huangwei.zhang@nus.edu.sg. Tel.: +65 6516 2557

ABSTRACT

Dynamics of ethylene autoignition and deflagration-to-detonation transition (DDT) are first numerically investigated in a one-dimensional shock tube using a reduced chemistry including 10 species and 10 reactions. Different combustion modes are investigated through considering various premixed gas equivalence ratios (0.2 – 2.0) and incident shock wave Mach numbers (1.8–3.2). Four ignition and DDT modes are observed from the studied cases, i.e., no ignition, deflagration combustion, detonation after reflected shock, and deflagration behind the incident shock. For detonation development behind the reflected shock, three autoignition hot spots are formed. The first one occurs at the wall surface after the re-compression of the reflected shock and contact surface, which further develops to a reaction shock because of “the explosion in the explosion” regime. The other two are off the wall, respectively, caused by the reflected shock/rarefaction wave interaction and reaction induction in the compressed mixture. The last hot spot develops to a reaction wave and couples with the reflected shock after a DDT process, which eventually leads to detonation combustion. For deflagration development behind the reflected shock, the wave interactions, wall surface autoignition hot spot as well as its induction of reaction shock are qualitatively similar to the mode of detonation after incident shock reflection, before the reflected shock/rarefaction wave collision point. However, only one hot spot is induced after the collision, which also develops to a reaction wave but cannot catch up with the reflected shock. For deflagration behind the incident shock, deflagration combustion is induced by the incident shock compression whereas detonation occurs after the shock reflection. The chemical timescale increases after the reflected shock/contact surface collision, whereas decreases behind the incident and reflected shocks, as well as after the reflected shock/rarefaction wave interaction. Therefore, mixture reactivity behind the reflected shock is weakened by the contact surface, but is intensified by the rarefaction wave. The multi-dimensionality characteristics, including reflected shock/boundary layer interactions, reflected shock bifurcation, destabilization, and detonation, are further present in a two-dimensional configuration. Planar autoignition occurs because of reflected shock compression and detonation combustion is formed first in the central region due to the collision of the reflected shock wave/reflected compression wave. The left and right bifurcations of the separation region in the wall boundary layer are then sequentially ignited.

Published under an exclusive license by AIP Publishing. <https://doi.org/10.1063/5.0103013>

I. INTRODUCTION

Due to the simplicity of geometrical configuration and convenience in controlling the thermodynamic conditions of the post-shock gas, shock tube experiments are popularly used to measure ignition delay time of various fuels¹ or investigate two-phase gas-droplet interactions.² Two essential characteristics of the gas dynamics in shock tubes (either reactive or non-reactive) are various wave interactions (e.g., those between reflected shock, contact surface, and rarefaction wave)^{3–5} and shock-boundary layer interactions.^{6–8} However, to prolong the test time usable in ignition delay measurements, “tailored”

driver-driven gas interface is widely used in previous shock tube studies, both experimentally^{9–11} and analytically.¹² In many numerical studies,^{13–17} the interactions between the reflected shock wave and incident contact surface as well as the rarefaction wave are also avoided deliberately. In these cases, the gas behind the reflected shock is not further disturbed by any wave interactions.

Nevertheless, the interactions between the reflected shock wave and contact surface as well as rarefaction wave may be important for the practical ignition behaviors of combustible gas.^{5,18} One-dimensional (1D) interaction of a detonation wave with a contact

discontinuity is investigated analytically and experimentally for the oxygen–hydrogen mixture.⁵ The results show that the shock can either be amplified or attenuated when it transmits through the contact surface and then propagates into an inert gas (helium/air mixture), depending on the reflection type at the contact surface as well as the ratio of acoustic impedance across it. The reflection type is found to depend on the ratio of internal energies across the contact surface.¹⁹ However, the ignition and combustion development of hydrocarbon fuels like ethylene, under complex wave interactions (include but are not limited to the shock/contact surface interaction), are still not fully understood from the above studies. Furthermore, the behavior of the shock when it further propagates into combustible mediums after its interaction with the contact surface and rarefaction wave has not been well investigated in the above studies.^{5,18,19}

Generally, two ignition modes, i.e., mild^{17,20,21} and strong (or sharp)^{22–24} ignitions, are observed both experimentally and numerically. According to Meyer and Oppenheim,²³ mild ignition starts from distinct flame kernels which grow slowly, whereas strong ignition is planar ignition that covers the cross-section of a shock tube instantaneously. In the work of Yamashita *et al.*,⁶ the ignition modes are classified as near-wall (strong) and far-wall (mild) ignitions. The local ignition hot spots in mild ignition are induced by the non-uniformity behind reflected shock waves,⁶ which can occur in, e.g., the boundary region near the sidewall of the shock tube,^{25–27} the bulk flow,^{28,29} or the both regions but with some delay in time.^{17,30} The switch between the different localized ignition modes is found to be sensitive to e.g., ignition temperature^{6,31,32} and shock wave intensity,^{8,33,34} which implies that different mechanisms may be responsible for the formation of ignition hot spot. Therefore, it is of interest to further investigate ignition and deflagration/detonation development under complex wave interactions for hydrocarbon fuels.

In this work, detailed numerical studies are performed to investigate the autoignition and deflagration-to-detonation transition (DDT) in ethylene/air mixtures subject to the shock wave reflection on the wall. A reduced ethylene mechanism is used, which includes 10 species and 10 reactions.³⁵ In the context of hydrocarbon fuels, ethylene is chosen here mainly because it is generally the major component from kerosene cracking reactions. The most famous kerosene surrogate may be the binary mixture of 36% CH₄ + 64% C₂H₄ in volume, which is primarily recommended to mimic the thermally or catalytically cracked JP-7 like fuels.³⁶ Different premixed gas equivalence ratios and incident shock wave Mach numbers are studied. 1D and two-dimensional (2D) domains are used with high mesh resolutions to capture the detailed and unsteady gas dynamics.

The novelties of this study are twofold. First, the multi-wave systems are considered, e.g., the incident shock wave, contact surface and rarefaction wave as well as their reflected counterparts. This differs from the previous work, e.g., Refs. 13, 14, and 37, which deliberately avoid the wave interactions and therefore their effects on combustion evolutions cannot not be reproduced. Second, automated reaction analysis based on chemical explosive mode analysis (CEMA)^{38–41} is performed through an eigen-decomposition of the chemical Jacobian matrix.^{39,42} This enables us to extract the quantitative chemical information behind the wave–chemistry interactions, which is not unveiled in the previous studies. The implication of this study for shock tube experiments mainly lies in understanding detailed scenario of the complex wave interactions, which are not readily to be obtained with

optical diagnostics. The high-fidelity numerical simulations enable detailed examination on the complicated autoignition and DDT phenomenon behind a reflected shock, which are generally challenging for measurement.

II. PHYSICAL PROBLEM

Autoignition and deflagration-to-detonation transition in combustible mixtures behind reflected shock waves with a semi-closed shock tube are studied. Figure 1(a) shows a schematic of the 1D computational domain, which starts at $x = 0$ and is 0.2 m long (x -direction). The length scale in y - and z -directions is 20 μm , which does not affect the results because the reduced directions (i.e., y - and z -directions for 1D cases and z -direction for 2D cases) are discretized with one cell, and the “empty” condition is applied (hence no numerical fluxes).⁴³ The left boundary is a reflective, adiabatic non-slip wall, whereas the right is a supersonic inlet with Dirichlet conditions enforced for all variables. The supersonic inlet gas enters the domain at the right end ($x = 0.2$ m) at $t = 0$, with an initial Mach number $M_{si,0}$. Its composition is identical to the mixture in the shock tube, which further naturally triggers a leading shock (i.e., incident shock wave) followed by a contact surface and a rarefaction wave [see Fig. 1(a)]. The interactions between the left wall and incident shock wave would lead to a right-propagating reflected shock wave and therefore second compression of the combustible mixture. The reflected shock may further interact with the incident contact surface and rarefaction wave as seen in Fig. 1(b), which schematically shows the evolutions of wave reflections and interactions. Details will be further presented for three representative cases in Sec. IV A. The strengths of the incident shock wave, contact surface, and rarefaction wave can be readily controlled by the supersonic inlet gas conditions. This further enables the investigation of various wave interactions with different patterns and strengths on the combustion mode and detonation evolution in practical shock tubes.

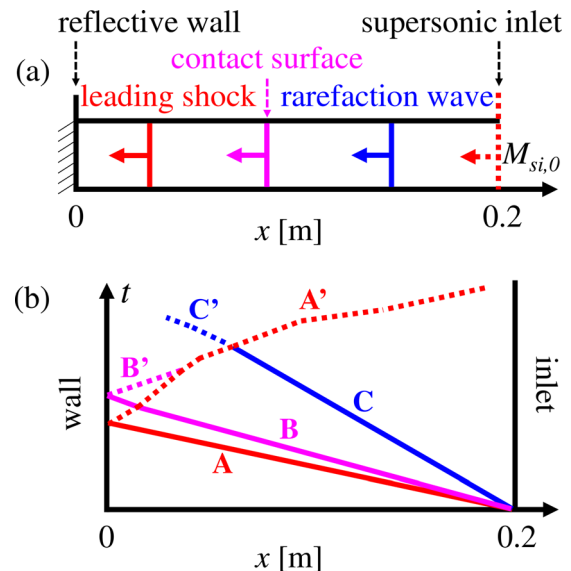


FIG. 1. Schematics of (a) the computational domain for a one-dimensional shock tube and (b) spatial-temporal evolutions of the leading shock, contact surface, and rarefaction wave.

TABLE I. Gas conditions corresponding to different inflow Mach numbers in stoichiometric ethylene/air mixture. $p_{si,0}/T_{si,0}$, $p_{sf,0}/T_{sf,0}$, and $p_{rs,0}/T_{rs,0}$ are, respectively, the pressures/temperatures at the inlet ($x = 0.2$ m), behind incident shock and reflected shock.

$M_{si,0}$	$p_{si,0}$ (kPa)	$T_{si,0}$ (K)	$p_{sf,0}$ (kPa)	$T_{sf,0}$ (K)	$p_{rs,0}$ (kPa)	$T_{rs,0}$ (K)
1.8	56.6	472.4	79.6	646.9	364.1	1009.8
2.0	77.4	509.2	104.6	751.7	540.9	1215.4
2.4	147.5	590.5	177.1	1036.8	1122.5	1774.7
2.8	285.2	680.2	289.7	1443.2	2144.1	2588.9
3.2	554.6	777.5	456.2	2009.1	3797.0	3743.1

Note that the multi-dimensionality effects in experimental shock tubes may be also important because of boundary layer growth and/or shock/boundary layer interactions, which further leads to non-uniform ignition.^{6,7,44} This will be examined through high-resolution two-dimensional simulations in Sec. IV C.

The initial gas composition in the shock tube is ethylene/air mixture with equivalence ratios of $\phi_0 = 0.2 - 2.0$. The initial pressure and temperature are, respectively, 10 kPa and 300 K. The inlet gas Mach numbers considered in this study are $M_{si,0} = 1.8, 2.0, 2.4, 2.8,$ and 3.2 . The gas conditions at the inlet, behind the incident shock, and behind the reflected shock for stoichiometric ethylene/air mixture (mass ratio $Y_{C_2H_4}/Y_{O_2}/Y_{N_2} = 0.064/0.218/0.718$) are detailed in Table I. Here, the studied conditions behind the reflected shock wave are comparable to the ethylene experiments of Penyazkov *et al.* ($p_{rs,0} = 5.9-16.5$ atm, $T_{rs,0} = 1060-1520$ K),⁹ Saxena *et al.* ($p_{rs,0} = 2, 10, 18$ atm, $T_{rs,0} = 1000-1650$ K),¹⁰ and Wan *et al.* ($p_{rs,0} = 0.97-20.54$ atm, $T_{rs,0} = 721-1307$ K).¹¹ Note that the gas conditions behind the incident and reflected shocks (e.g., $p_{sf,0}/T_{sf,0}$ and $p_{rs,0}/T_{rs,0}$ respectively) are naturally resulted from the supersonic inlet gas. They are read from non-reactive simulations under the identical inlet conditions to those in the reactive cases.

III. NUMERICAL METHOD AND COMPUTATIONAL DIAGNOSTIC TOOL

A. Numerical method

The governing equations of mass, momentum, energy, and species mass fractions are solved for compressible, multi-species, reacting flows. The governing equations are solved by a density-based multi-component reactive flow solver, *RYrhoCentralFoam*.^{43,45,46} It is developed from *rhoCentralFoam* solver in OpenFOAM 5.0 package.⁴⁷ The *RYrhoCentralFoam* solver is verified and validated with a series of benchmark cases against analytical solutions and/or experimental data in our recent work.^{43,48} It can accurately predict gaseous detonation properties in different fuels (e.g., hydrogen and methane), including reaction-shock interaction, propagation speed, frontal structures, and cell size.⁴³ Recently, it is successfully used for simulations of supersonic combustion and detonations.^{43,46,48}

A second-order implicit Crank – Nicolson scheme⁴⁹ is used for temporal discretization. A Godunov-type Riemann-solver-free scheme developed by Kurganov *et al.*⁵⁰ is used, with Minmod flux limiter⁵¹ for convective fluxes for accurate shock capturing. The diffusive fluxes are predicted with a second-order central differencing scheme.⁵² The physical time step is $10^{-9} - 10^{-10}$ s. Detailed information about the equations and numerical method can be found in Refs. 43, 45–48, and 53.

The stiff ODE solver *seulex*⁵⁴ is used to integrate the chemical reaction system. A reduced chemical mechanism for ethylene combustion is used, which contains 10 species ($C_2H_4, O_2, CO, H_2, O, CO_2, OH, H, H_2O,$ and N_2) and 10 reactions.³⁵ The Arrhenius kinetic parameters can be found in Ref. 35, whilst the thermodynamic ones are estimated with JANAF polynomials.⁵⁵ This mechanism is validated against the detailed mechanism (25 species and 77 reactions, assembled from the experimental data in Ref. 56) over a range of operating conditions, and the results agree well with the measured data for, e.g., evolutions of temperature, pressure and key species concentrations.³⁵ It is used for simulations of supersonic flames^{57,58} and detonations.^{59,60} Comparisons of ignition delay time and constant volume ignition profiles with experimental data as well as detailed mechanism are provided in Sec. A of the supplementary material. It is found that this mechanism preserves acceptable accuracies with least computational cost compared with the detailed mechanisms, which exhibits the high-cost-benefit ratio for high mesh resolutions (e.g., $10 \mu\text{m}$ in the present study).

Furthermore, a representative case with $\phi_0 = 1.0$ and $M_{si,0} = 2.0$ (see Table I) is simulated with both the reduced mechanism³⁵ and the detailed one of Wang and Laskin (75 species and 529 reactions).⁶¹ Comparison of the results is provided in Sec. B of the supplementary material, and it is found that the major characteristics including wave interactions and final stable detonation zone are close for the two mechanisms.

Three uniform meshes with 10 000, 20 000, and 40 000 cells are adopted to discretize the 1D domain in Fig. 1(a). They correspond to the cell sizes of 20, 10, and $5 \mu\text{m}$, respectively. The grid dependence analysis is provided in Sec. C of the supplementary material, and it is found that the differences in autoignition and DDT development with three meshes are negligible. Therefore, in the subsequent analysis, the resolution of $10 \mu\text{m}$ is used. This leads to about 98 cells in the half-reaction zone of Chapman–Jouguet (C–J) detonation under the conditions behind the reflected shock wave with $M_{si,0} = 2.0$ (see Table I).

B. Chemical reaction analysis

CEMA^{38–41} is an automated approach for studying ignition and detonation development in premixed gas. It can extract the comprehensive reaction information from local chemical Jacobian matrix.^{39,42} For a reaction system, the evolutions of thermochemical composition follow:

$$\frac{D\boldsymbol{\varphi}}{Dt} = \mathbf{g}_\omega(\boldsymbol{\varphi}) + \mathbf{s}(\boldsymbol{\varphi}), \quad (1)$$

where $\boldsymbol{\varphi} = (c_1, c_2, \dots, c_N, T)$ is the vector of species molar concentrations c_i and temperature T from the detailed reactive flow simulations. $D(\cdot)/Dt$ is the material derivative. The term $\mathbf{g}_\omega(\boldsymbol{\varphi})$ is the vector of chemical source terms, whereas $\mathbf{s}(\boldsymbol{\varphi})$ denotes all the non-chemical terms. In CEMA method, eigen-analysis of the local chemical Jacobian matrix is performed,^{39,40,42} i.e.,

$$\frac{D\mathbf{g}_\omega(\boldsymbol{\varphi})}{Dt} = J \cdot \frac{D\boldsymbol{\varphi}}{Dt} = J \cdot [\mathbf{g}_\omega(\boldsymbol{\varphi}) + \mathbf{s}(\boldsymbol{\varphi})], \quad (2)$$

where $J = \frac{\partial \mathbf{g}_\omega(\boldsymbol{\varphi})}{\partial \boldsymbol{\varphi}}$ is the local chemical Jacobian matrix. Chemical modes are associated with the eigenvalues of J , among which the one

with the maximum real part is denoted as λ_e . A chemical explosive mode is identified when the real part of λ_e , $Re(\lambda_e)$, is positive.

The contribution of species or temperature to a CEM is quantified through explosion index,^{39,42} i.e.,

$$EI_j = \max\{\text{sign}[Re(\lambda_e)], 0\} \cdot \frac{\text{diag}|\mathbf{l}_e \mathbf{r}_e|_j}{\sum_{i=1}^{N+1} \text{diag}|\mathbf{l}_e \mathbf{r}_e|_i}, \quad (3)$$

where $\text{sign}(x)$ and $\max(x,y)$ are, respectively, the sign and maximum functions, $\text{diag}|\cdot|_j$ is the absolute value of diagonal element for j -th variable, \mathbf{l}_e and \mathbf{r}_e are the left and right eigenvectors corresponding to λ_e . EI_j closes to 1 means that the corresponding variable (species concentration or temperature) is dominant in the CEM. Full details of the CEMA method can be found in Refs. 39, 40, and 42.

IV. RESULTS AND DISCUSSION

A. Combustion mode

Four combustion modes of ethylene/air mixtures subject to incident/reflected shock waves are observed based on our simulation results: (1) no ignition, (2) deflagration combustion behind reflected shock, (3) detonation combustion behind reflected shock, and (4) deflagration combustion behind the incident shock wave (also develops to detonation after the shock is reflected at the wall). A combustion mode map is shown in Fig. 2, which is parameterized by premixture equivalence ratio and inflow Mach number. These two global parameters are the direct reasons that determine the patterns and strengths of various wave interactions. However, the various wave interactions further physically affect the evolution of different combustion modes. It is found that under low inflow Mach numbers and/or low equivalence ratios, modes 1 (e.g., $M_{si,0} \leq 1.8$, or $M_{si,0} = 2.0$ but $\phi_0 \leq 0.4$) and 2 (two cases with $M_{si,0} = 2.0$ and $\phi_0 = 0.6$, $M_{si,0} = 2.4$ and $\phi_0 = 0.2$) are more likely to occur. Mode 3 becomes more prevalent when the inflow Mach number is further increased. When $M_{si,0} = 3.2$, mode 4 occurs

- no ignition
- deflagration behind reflected shock
- ▲ detonation behind reflected shock
- ▼ deflagration behind incident shock

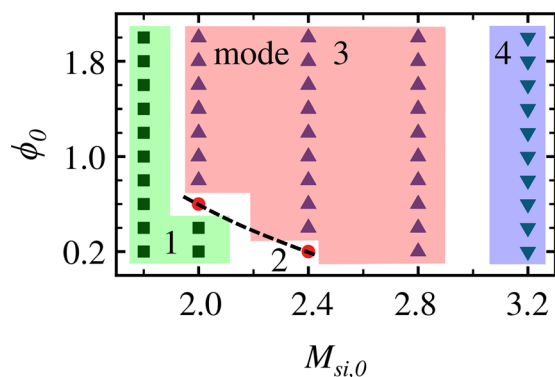


FIG. 2. Diagram of the combustion modes in ethylene/air mixture subject to incident/reflected shocks. The numbers indicate four combustion modes.

for all the considered equivalence ratios. One can also see that the dependence of combustion mode on the mixture equivalence ratio is weaker than that of inflow Mach number. For instance, when ϕ_0 is above 0.8, the predicted modes in Fig. 2 are solely affected by the $M_{si,0}$. In the following, detailed transients in combustion modes 2 – 4 and the underlying interactions between chemical reaction and gas dynamics will be discussed through the representative cases.

It is worth noting that all detonation waves in the 1D simulations, when applicable, are stable for the studied conditions in the present work. No pulsating detonation is observed, which however, has been found in our recent work for *n*-heptane/air mixture,⁶² and in Ref. 63 for hydrogen/oxygen mixture. Furthermore, both explosion and detonation limits of the ethylene/air mixture are extended under the high temperature and pressure conditions behind the reflected shock wave (see Table I). This makes detonation possible when $M_{si,0} \geq 2.8$ with $\phi_0 = 0.2$. As a reference, the explosion limit of ethylene in the ambient air is 2.7%–36% in volume.⁶⁴

1. Autoignition and detonation development

Figure 3 shows the evolutions of pressure gradient, pressure, temperature, and heat release rate in x - t diagram. In the following, the white zones in variable contours are clipped by the lower limit of the shown legend for readability. The initial conditions are $M_{si,0} = 2.0$ and $\phi_0 = 1.0$, which corresponds to mode 3. In Fig. 3(a), the incident shock wave A impinges on the wall at point a ($t \approx 193 \mu\text{s}$) and is reflected (shock wave D). The latter intersects with incident contact surface B at point b ($x \approx 16.2 \text{ mm}$ and $t \approx 239 \mu\text{s}$), and both are decelerated after they collide. The reason will be further discussed in Sec. IV B. Then, a reflected shock is generated due to the collision of A/B, which further impinges on the wall at point d ($t \approx 255 \mu\text{s}$), and a wall-reflected shock (hereafter, it is termed as reflected compression wave to distinguish it from many other waves and their reflections) F is formed.^{5,18} It subsequently merges with the transmitted shock D at point e ($x \approx 35.8 \text{ mm}$ and $t \approx 314 \mu\text{s}$) and D is intensified because the pressure gradients of F and D are in the same direction.

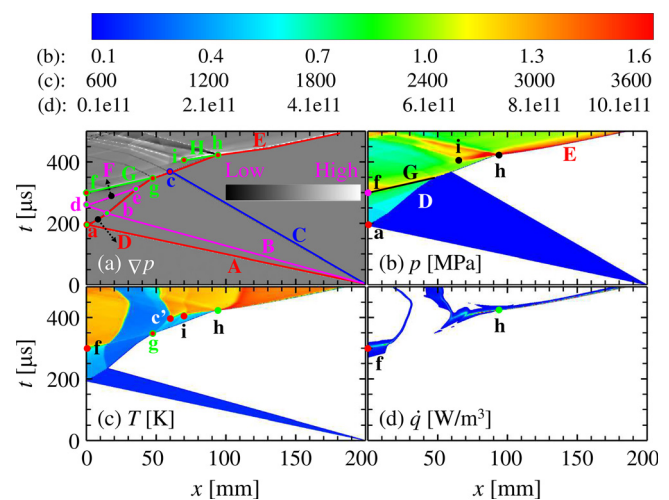


FIG. 3. x - t diagrams of (a) pressure gradient, (b) pressure, (c) temperature, and (d) heat release rate. $M_{si,0} = 2.0$ and $\phi_0 = 1.0$, mode 3.

Moreover, a shock wave G is induced at point f ($t \approx 302 \mu\text{s}$). This is caused by “the explosion in the explosion,”^{9,14,65} i.e., the near-wall autoignition hot spot f induced by the shock compression, manifested by locally high pressure, temperature, and heat release rate in Figs. 3(b)–3(d), respectively. This reaction shock G propagates toward the shocked gas, and then catches up with the reflected shock D at point g ($x \approx 47.4 \text{ mm}$ and $t \approx 348 \mu\text{s}$) and part of it is reflected back (see the backward propagating bifurcation at point g). Nevertheless, the reflected shock D is slightly intensified after point g (flatter slope of the trajectory), which then collides with the incident rarefaction wave C at point c ($x \approx 59.8 \text{ mm}$ and $t \approx 366 \mu\text{s}$). Both waves are intensified, and a second reactive hot spot c' is initiated, which originates from D–C collision location c.

A third reactive hot spot appears in the compressed mixture at point i ($x \approx 70.2 \text{ mm}$ and $t \approx 406 \mu\text{s}$), which generates two bifurcated, right- and left-running, reaction waves. The former reaction wave, H, catches up with D at point h ($x \approx 93.0 \text{ mm}$ and $t \approx 423 \mu\text{s}$) after a DDT process. D and H mutually enhance and couple with each other, thereby generating a new detonation wave E at point h. The propagating speed of detonation wave E is 1787 m/s, which is close to the C–J speed (1797 m/s based on the gas conditions behind the incident shock, see Table I). Note that the interactions between the reflected shock wave with reflected compression wave only make sense after point e where they collide. This collision has little influence on the near-wall mixture. Furthermore, the reflection of rarefaction wave on the wall is of no interest because at that time the detonation wave E almost gets out of the domain.

Figure 4 shows the chemical explosive mode and explosion indices [Eq. (3)] of temperature and dominant species (i.e., OH and O radicals) in x - t diagrams. The CEM is visualized through

$$\lambda_{cem} = \max\{\text{sign}[Re(\lambda_e)], 0\} \cdot \log_{10}\left[1 + |Re(\lambda_e)|\right]. \quad (4)$$

In Fig. 4(a), only the mixture roughly between the incident shock A and contact surface B is chemically explosive before the shock reflection on the wall. However, λ_{cem} is relatively low there, which indicates

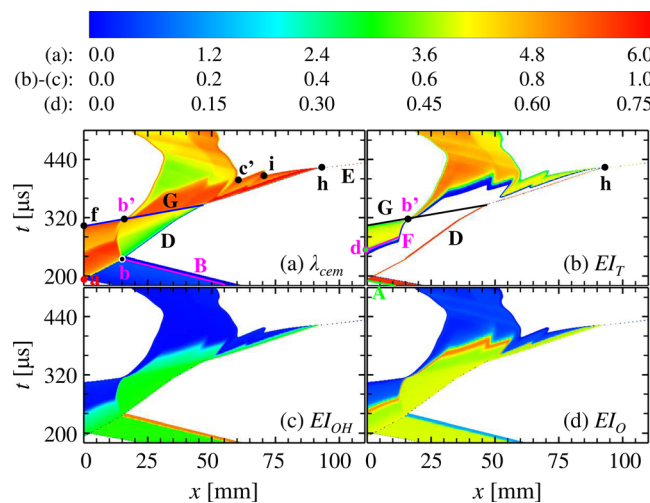


FIG. 4. x - t diagrams of (a) CEM distribution and explosion indices for (b) temperature, (c) OH, and (d) O radicals.

that the chemical timescales are large (say, above 1 s). After the reflected shock wave, the near-wall mixture (before point b) is found to have increased propensity of chemical explosion (high λ_{cem}), sequentially experiencing chemical runaway (or chain-branching reactions), thermal runaway, and ultimate autoignition (i.e., point f), as can be seen from Figs. 4(b) to 4(d). Note that chemical (thermal) runaway corresponds to a high dependence on radical species (temperature). It is also seen that on the left side of point b', across the reaction shock G the chemical mode abruptly transitions from explosive one to dissipative one (white area, i.e., the slowest decaying mode in a non-explosive mixture^{39,40}). Moreover, a significant increase in λ_{cem} is observed behind G, on the right side of point b', with high chemical runaway and hence strong chain-branching reactions [see explosion indices for OH and O in Figs. 4(c) and 4(d)]. As time increases, thermal runaway propensity becomes significant, ultimately generating the second and third hot spots, c' and i [see Figs. 3(b) and 3(c)]. When detonation is developed, the CEM region is only observed in the induction zone of the detonation wave E, which is consistent with the observations from two-dimensional detonation structures.⁶⁶

In addition, there is also a distinct boundary between chemical runaway and thermal runaway (starts at $t \approx 248 \mu\text{s}$ on the wall), right below line F as seen in Fig. 4. This is a natural transition process caused by the reaction induction in the near wall region after the incident shock reflection point a. However, it happens right before point d where the compression wave is reflected. Above line F, λ_{cem} gradually increases again. This will be further confirmed in Figs. 5 and 11.

To further elaborate on the interactions between the gas dynamics and chemical reactions, Fig. 5(a) shows the evolutions of chemical timescale, t_e (i.e., the reciprocal of $|Re(\lambda_e)|$ from CEM³⁹) at $x = 0, 47.4,$

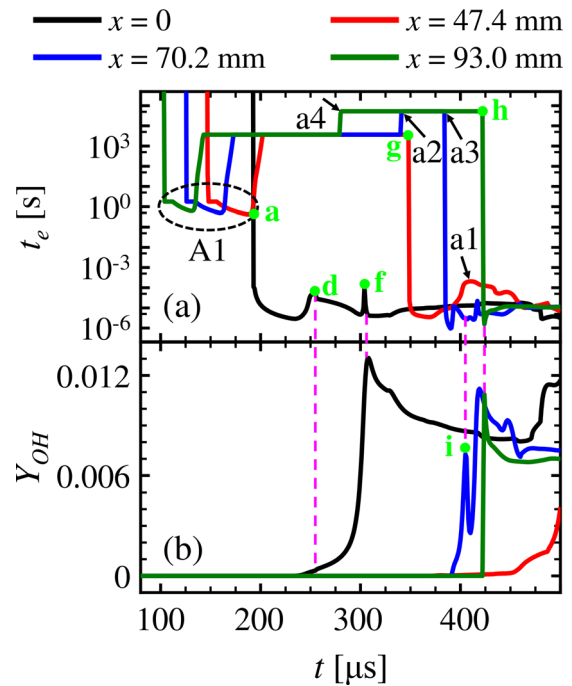


FIG. 5. Evolutions of (a) chemical timescale (in logarithmic scale) and (b) OH mass fraction at various locations. Letter symbols same as in Figs. 3 and 4.

70.2, and 93.0 mm, which, respectively, correspond to the locations of points a, g, i, and h in Fig. 3(a). Figure 5(b) shows the evolutions of OH mass fraction Y_{OH} at these locations. In Fig. 5(a), the mixture is not chemical explosive (e.g., $t_e > 10^5$ s) before the incident shock wave arrives. When the incident shock wave sweeps the four locations at $t \approx 193, 148, 126,$ and $104 \mu\text{s}$, respectively, there is a sharp decrease in t_e , to about 1 s (indicated by A1). However, t_e recovers to above 10^3 s after the incident contact surface passage (at $t \approx 203, 173,$ and $143 \mu\text{s}$) for the latter three points. For the wall surface $x=0$, it is re-compressed by the reflected shock wave, and t_e decreases to about 10^{-5} s (i.e., after point a). Then, t_e slightly increases due to thermal expansion from combustion heat release (not observable in Fig. 3(d) because \dot{q} is clipped below 10^{10} W/m^3 , which however actually exists and leads to decreased wall pressure). This ends at point d, when the compression wave [generated due to the collision between the reflected shock wave and incident contact surface at point b in Fig. 3(a)] is reflected on the wall. The mixture is compressed again and therefore t_e decreases. Meanwhile, the OH radical rapidly increases after d and peaks at f, where finally the first autoignitive spot is formed as seen in Fig. 3(a). After that, slow recombination reactions proceed and t_e nearly keeps constant whereas OH is slowly reacted.

For $x = 47.4 \text{ mm}$, t_e sharply decreases from above 10^3 s (i.e., the state behind the incident contact surface), to about 10^{-5} s [the state behind G in Fig. 3(a)] at point g. Then, t_e slowly decreases because of continuous chain-branching reactions, but it peaks at $t \approx 409 \mu\text{s}$ (a1) because the combustion is weakened by the incident rarefaction wave. After that, t_e slowly decreases, whereas OH radical is slowly built up, indicating lasting reaction induction at this location.

For the reactive hot spot at $x = 70.2 \text{ mm}$, the chemical timescale t_e increases to above 10^4 s behind the incident rarefaction wave at $t \approx 343 \mu\text{s}$ (a2), which ends when the reflected shock wave D arrives here at $t \approx 384 \mu\text{s}$ (a3). Meanwhile, pronounced OH radical occurs since then, which peaks when the autoignitive spot occurs at point i. There is another peak of Y_{OH} after point i, which is caused by the left-propagating reaction wave originated from point h [see Fig. 3(a)]. For the detonation initiation location at $x = 93.0 \text{ mm}$, it also experiences the influences of incident shock wave and contact surface, as well as incident rarefaction wave [$t \approx 281 \mu\text{s}$, a4 in Fig. 5(a)]. Then, t_e decreases to about 10^{-6} s while Y_{OH} sharply increases at point h, when the detonation flame front is formed.

2. Deflagration flame propagation

Figure 6 shows the evolutions of pressure gradient, pressure, temperature, and heat release rate in $x-t$ diagram. The initial conditions are $M_{si,0} = 2.0$ and $\phi_0 = 0.6$, which corresponds to mode 2. Different from the stoichiometric results in Sec. IV A 1, in this case, only deflagration combustion is developed after the reflected shock wave. The interactions between the leading shock, contact surface, rarefaction wave and their reflections on the wall, as well as the reaction shock wave G before point c are qualitatively similar to those discussed in Sec. IV A 1. After point c, only one hot spot is present, which can be seen from Fig. 6(c). The right-running reaction wave cannot catch up with the leading shock to support a propagating detonation, before the latter arrives at the right end. In Fig. 6(a), it is seen that the reaction front (the white zone following D) significantly lags behind D. With further decreased equivalence ratio (e.g., $\phi_0 = 0.2$), there is even no

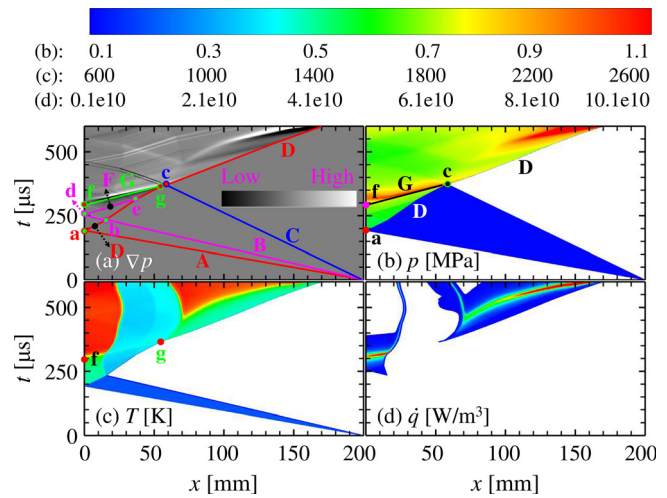


FIG. 6. $x-t$ diagrams of (a) pressure gradient, (b) pressure, (c) temperature, and (d) heat release rate. $M_{si,0} = 2.0$ and $\phi_0 = 0.6$, mode 2.

propagating reaction front behind the leading shock (off the wall, no hot spot can be formed), and only the near-wall mixture burns after shock compression.

Figure 7 shows the chemical explosive mode and explosion indices of temperature and dominant species in $x-t$ diagram. In Figs. 7(a)–7(d), the evolutions of λ_{cem} , EI_T , EI_{OH} , and EI_O are qualitatively similar to the counterparts in Fig. 4 before point c. Beyond point c, the CEM regions exist between the leading shock and reaction wave [see Fig. 7(a)]. Within these regions, there are two stages, i.e., first chemical runaway (high EI_{OH} or EI_O values) immediately behind the shock wave and then thermal runaway (high EI_T values) ahead of the reaction wave. A sharp increase in gas temperature and pressure is resulted from the compression of the reflected shock wave. Chain-branching reactions (i.e., those producing intermediate species like OH and O radicals)

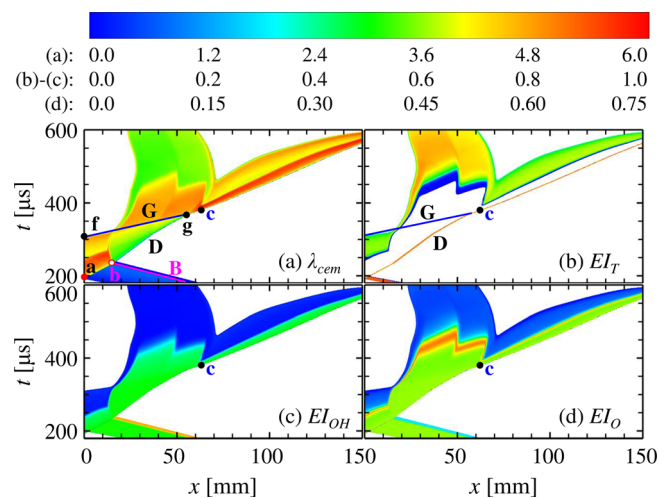


FIG. 7. $x-t$ diagrams of (a) CEM distribution and explosion indices for (b) temperature, (c) OH, and (d) O radicals.

have a strong propensity to occur. Therefore, chemical runaway is first observed right behind the shock front. As chain-branching reactions proceed, remarkable heat release rate starts to occur toward the reaction wave [see Fig. 6(d)]. The mixture has a strong propensity of autoignition after some distance of reaction induction. Thermal runaway is then observed until the mixture is fully autoignited at the reaction wave front. They can be observed from the local explosion indices of species and temperature, respectively, in Figs. 7(b)–7(d). The reaction front has a propensity to catch up with the leading shock D. However, they are still not fully coupled within the computational domain. It is worth noting that when the shock tube is sufficiently long, say 1 m for this case, it is possible to finally achieve detonation combustion.

Figure 8 further shows the evolutions of chemical timescale and OH mass fraction at $x = 0$, 15.1, and 55.8 mm, which, respectively, correspond to the locations of points a, b, and g in Fig. 6(a). In Fig. 8(a), the mixture is not chemically explosive (e.g., $t_e > 10^5$ s) before the incident shock wave arrives. When the incident shock reaches the three locations at $t \approx 192$, 178, and 139 μs , respectively, t_e sharply decreases to about 1 s. For the wall surface $x = 0$, it is similar to the results in Fig. 5. For $x = 15.1$ mm, t_e slowly decreases after the incident shock wave passage because slow reactions with weak heat release are induced behind the shock (see Fig. 7). At point b, t_e sharply decreases from above 0.4 s (i.e., the developing state behind the incident shock wave), to about 10^{-5} s (the state that is sequentially compressed by the incident shock wave and contact surface). Then, t_e slowly increases and decreases because of continuous chain-branching reactions, but it peaks at $t \approx 322$ μs (a1), affected by the reaction shock wave G. After that, t_e slowly increases, whereas OH radical is slowly dissociated,

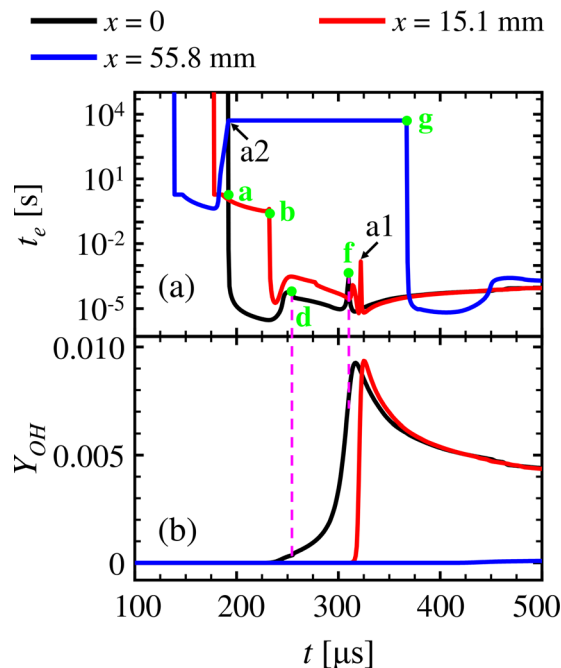


FIG. 8. Evolutions of (a) chemical timescale (in logarithmic scale) and (b) OH mass fraction at various locations. Letter symbols are same as in Figs. 6 and 7.

indicating a quasi-stable state after a deflagration flame passage. This is similar to the evolution of t_e after point f at location $x = 0$.

For $x = 55.8$ mm, t_e increases above 10^3 s behind the incident contact surface at $t \approx 192$ μs (a2), which ends when the reflected shock wave D and reaction shock wave G intersect here at $t \approx 366$ μs (i.e., point g). The chemical timescale drops to about 10^{-6} s behind g and mildly evolves as the second hot spot is slowly induced [see Fig. 6(c)]. However, unlike the similar point g in the stoichiometric case in Fig. 5, no pronounced Y_{OH} occurs till $t = 500$ μs as no detonation is developed.

3. Deflagration behind incident shock

Figure 9 shows the counterpart results for $M_{st,0} = 3.2$ and $\phi_0 = 1.0$ from mode 4. In this case, deflagration flame even occurs behind the incident shock wave, and detonation combustion is formed shortly after the reflected shock enters the combustible mixture behind the incident contact surface. In some studies, this is called the shock-induced detonation.^{67–69} In Fig. 9(a), the incident shock wave A reflects on the wall at point a ($t \approx 86$ μs). The reflected shock wave D then interacts with the incident contact surface B at point b ($x \approx 12.5$ mm and $t \approx 105$ μs) and both waves are decelerated. From points a to b, there is no obvious heat release because the mixture there is fully burned by the deflagration flame developed behind the incident shock wave A [see the high temperature between lines A and B in Fig. 9(c)]. This differs from the lower incident shock Mach numbers in Figs. 3 and 6, where no flame occurs before the incident shock reflection. However, a deflagration flame is again immediately developed once D enters the unburned mixture behind B as seen from the heat release rate distributions in Fig. 9(d). At point e ($x \approx 15.6$ mm and $t \approx 132$ μs), the shock front is significantly intensified when it collides with the reflected compression wave F. Coupling between the reaction front and shock front occurs, leading to a developing detonation G. Although the detonation front may further interact with other waves (e.g., slightly intensified by the collision with incident rarefaction wave C at point c), it can propagate in a self-sustainable manner.

Note that the near-wall temperature is extremely high (~ 4800 K) in Fig. 9(c), caused by the repeat compression from various waves and their reflections on the wall. The local mixture may not be treated as calorically perfect gas. However, this situation is ameliorated by two factors in present work. First, this high-temperature region almost stays near the wall, which has little influence on the initiation and development of the traveling detonation front far from the wall. Second, except this near-wall region, the gas temperature is much lower even behind the detonation wave [about 3700 K after point e in Fig. 9(c)]. Actually, the detonation front propagates in a medium that is only compressed by the rarefaction wave after point c, where the pre-detonation gas pressure and temperature are much lower than that right behind the reflected shock wave near the wall (see Table I).

Figure 10 further shows the evolutions of chemical timescale and OH mass fraction at $x = 0$, 12.5, and 15.6 mm, which, respectively, correspond to the locations of points a, b, and e in Fig. 9(a). In Fig. 10(a), t_e is considerably reduced to about 7×10^{-6} s when the incident shock arrives at these locations at $t \approx 86$, 81, and 80 μs , respectively. For the wall surface, t_e further drops to below 5×10^{-8} s because of the shock reflection on the wall. Meanwhile, Y_{OH} also increases at point a in Fig. 10(b). After the shock reflection, t_e increases to 3×10^{-7} s and Y_{OH} generally levels off over the period of interest. At $t \approx 113$ μs (arrow a1),

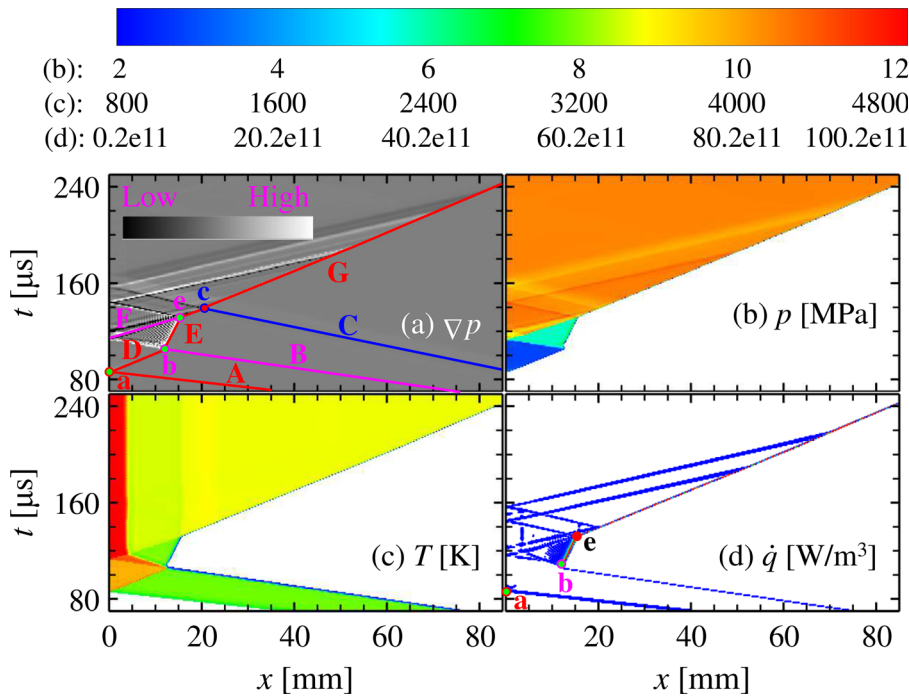


FIG. 9. x - t diagrams of (a) pressure gradient, (b) pressure, (c) temperature, and (d) heat release rate. $M_{si,0} = 3.2$ and $\phi_0 = 1.0$, mode 4.

t_e drops again to about 4.5×10^{-8} s, because the mixture is further compressed by the reflected compression wave.

For $x = 12.5$ mm, t_e is slightly increased at point b, but soon decreases as a deflagration flame is still sustained as seen in Fig. 9(d).

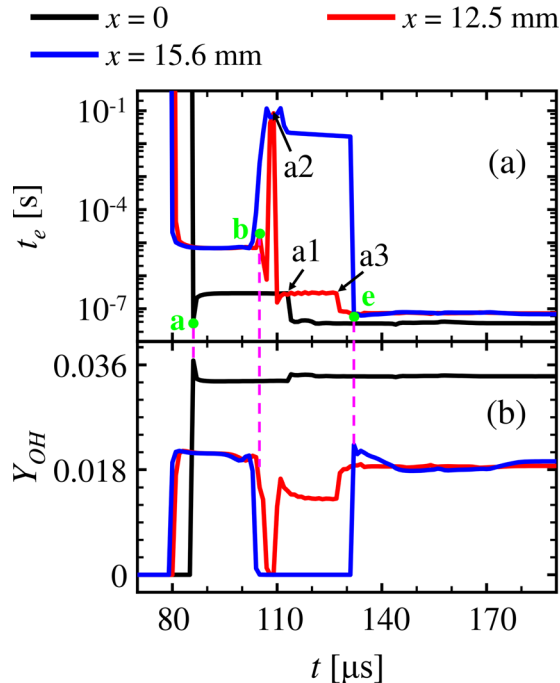


FIG. 10. Evolutions of (a) explosion timescale (in logarithmic scale) and (b) OH mass fraction at various locations. Letter symbols same as in Fig. 9.

Then, t_e increases to about 0.1 s at $t \approx 109 \mu\text{s}$ (arrow a2) because of the contact surface. Shortly, the unburned mixture is ignited by the reflected compression wave F and is fully burned at $t \approx 127 \mu\text{s}$ (arrow a3), both t_e and Y_{OH} tend to be stable. For $x = 15.6$ mm, the unburned mixture behind the incident contact surface is directly detonation combusted by the interaction of reflected shock wave E and reflected compression wave F at point e.

B. Further interpretations about wave interaction effects on chemical reaction

In the above section, it is found that interactions between the reflected shock wave and contact surface, as well as rarefaction wave, have significant effects on hot spot formation and reaction front development. Therefore, how they affect the chemical reactions behind these unsteady events will be further investigated in this section based on one representative case in Sec. IV A 1, i.e., with $M_{si,0} = 2.0$ and $\phi_0 = 1.0$.

Figure 11 shows the evolutions of pressure, temperature, velocity, and chemical timescale, before and after shock wave/contact surface collision [i.e., at point b in Fig. 3(a), $t \approx 239 \mu\text{s}$]. Note that across a contact surface, pressure and velocity are continuous [see Figs. 11(a) and 11(c)], whereas temperature and density are not (temperature decreases seen in Fig. 11(b) and density increases). The pressure ratio across a normal shock reads (in shock reference frame)⁷⁰

$$\frac{p_2}{p_1} = \frac{2k}{k+1} (Ma_1^2 - 1) + 1, \tag{5}$$

where the subscripts “1” and “2,” respectively, denote the parameters before and behind the shock front, and k is the specific heat ratio (here assumed to be constant for simplicity). Before the two-wave collision, the reflected shock wave propagates in the medium compressed by the

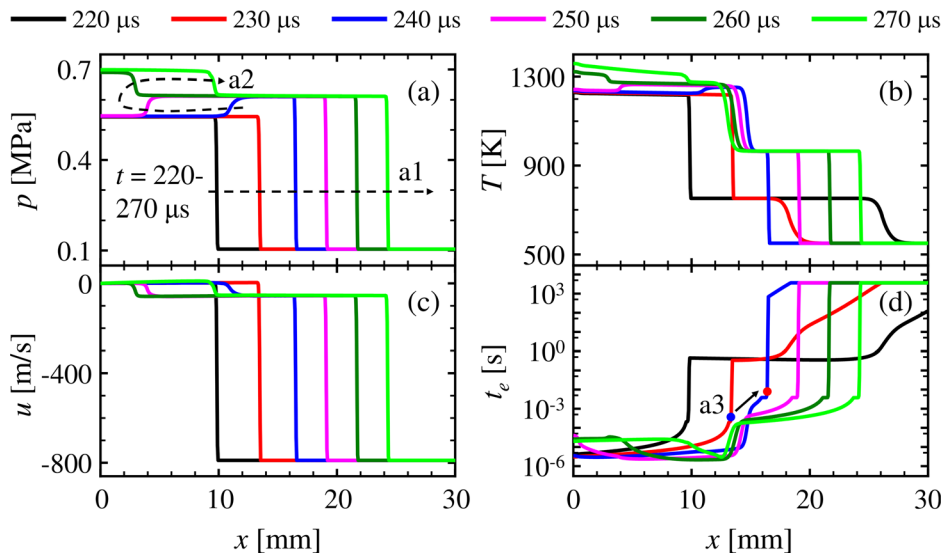


FIG. 11. Evolutions of (a) pressure, (b) temperature, (c) velocity, and (d) chemical timescale, before ($t \leq 230 \mu\text{s}$) and after ($t \geq 240 \mu\text{s}$) the reflected shock wave/incident contact surface interaction. $M_{si,0} = 2.0$ and $\phi_0 = 1.0$. Arrows a1 and a2 indicate the propagation direction of reflected shock wave front and contact surface (after collision), respectively.

incident shock wave, with $p_1 = 104.6 \text{ kPa}$ and $T_1 = 751.7 \text{ K}$. However, after collision, they are changed to $p_1 = 104.6 \text{ kPa}$ and $T_1 = 550.5 \text{ K}$, swept by the contact surface. Therefore, after wave collision, the reflected shock propagates into a denser but colder gas. In Fig. 11(a), it is found that the pressure ratio (p_2/p_1) is increased after the collision (e.g., increased from 5.21 to 5.87, from $t = 230$ to $240 \mu\text{s}$). Therefore, the pressure behind the reflected shock (p_2) is also increased as p_1 remains unchanged across the contact surface. According to Eq. (5), the shock Mach number, Ma_1 , is increased after collision.

In addition, the temperature ratio across a normal shock reads⁷⁰

$$\frac{T_2}{T_1} = \frac{[2kMa_1^2 - (k-1)][(k-1)Ma_1^2 + 2]}{(k+1)^2Ma_1^2}. \quad (6)$$

Hence, the temperature ratio (T_2/T_1) is also increased with Ma_1 after the collision. In Fig. 11(b), T_2/T_1 is increased from 1.62 to

1.75 when the two waves collide. However, before the collision, $T_1 = 751.7 \text{ K}$ (behind the incident shock), whereas after that, $T_1 = 550.5 \text{ K}$ (behind the contact surface). The pronounced decrease in pre-shock gas temperature leads to significant decrease in T_2 after collision, as seen from Fig. 11(b). From 230 to $240 \mu\text{s}$, the temperature behind the reflected shock wave decreases from 1218.8 to 965.3 K. The pronounced decrease in post-shock temperature leads to the significant increase in chemical timescale, and hence after collision, the reflected shock is weakened in chemical reactivity [see the increased t_e from 230 to $240 \mu\text{s}$, right behind the shock front indicated by a3 in Fig. 11(d)].

Figure 12 shows the evolutions of pressure, temperature, velocity, and chemical timescale, before and after the reflected shock wave/incident rarefaction wave collision [i.e., at point c in Fig. 3(a), $t \approx 366 \mu\text{s}$]. It is well known that across a rarefaction wave, pressure, temperature, and density decrease, whereas the velocity magnitude increases.

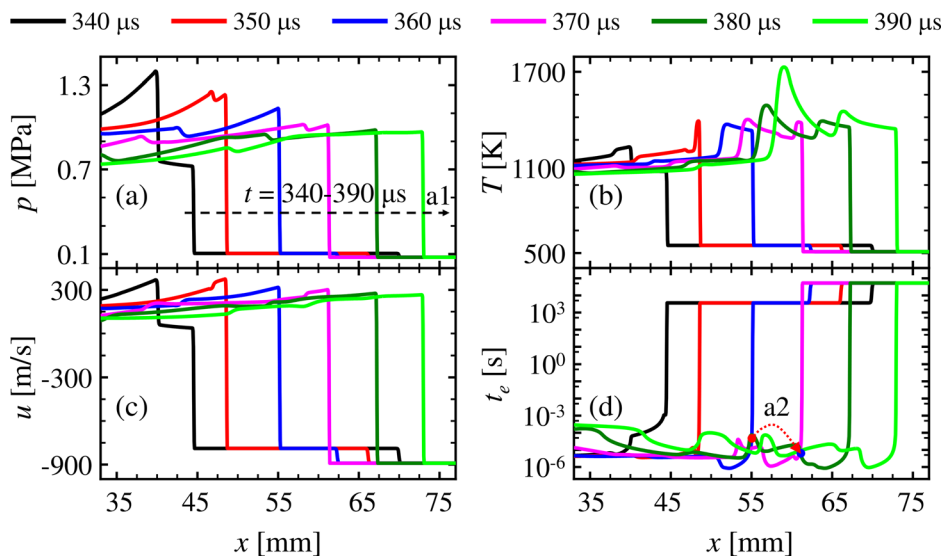


FIG. 12. Evolutions of (a) pressure, (b) temperature, (c) velocity, and (d) chemical timescale, before ($t \leq 360 \mu\text{s}$) and after ($t \geq 370 \mu\text{s}$) the reflected shock wave/incident rarefaction wave interaction. $M_{si,0} = 2.0$ and $\phi_0 = 1.0$.

The density, pressure and temperature ratios across the reflected shock are also determined by Eqs. (5) and (6). Before interaction, the shock wave propagates in the medium that is compressed by the incident contact surface, with $p_1 = 104.6$ kPa and $T_1 = 550.5$ K. After wave collision, the reflected shock propagates in the medium behind the rarefaction wave, with $p_1 = 77.4$ kPa and $T_1 = 509.2$ K. This also indicates a decreased speed of sound in the pre-shock gas after collision. Furthermore, it is found that the propagation speed of the reflected shock increases after the collision, e.g., $u_{sf} = 1414.1$ and 1490.6 m/s at $t = 360$ and $370 \mu\text{s}$, respectively. This means that the pre-shock Mach number relative to the shock front increases (i.e., $Ma_1 \uparrow$ because $u_1 \uparrow$, whereas $a_1 \downarrow$). Based on Eqs. (5) and (6), the pressure and temperature ratios all increase after collision. However, it does not mean that the pressure and temperature behind the shock front increase accordingly, because those in front of the shock front all decrease after the collision. Actually, the pressure and temperature behind the shock, respectively, change from 113.5 kPa and 1312.1 K to 101.5 kPa and 1363.5 K, from $t = 360$ and $370 \mu\text{s}$. The chemical reactivity behind the reflected shock increases [see the decreased t_c from $t = 360$ to $370 \mu\text{s}$, behind the shock front indicated by a2 in Fig. 12(d)] with the post-shock temperature after collision. These justify why the reflected shock is intensified through colliding with the incident rarefaction wave, as observed in Sec. IV A. The phenomena unveiled from Figs. 11 and 12 are also true for the reactive cases in Fig. 2.

Theoretical analysis on the interaction between a shock wave and a contact surface has been performed previously.^{5,18,19} It has been found that the transmitted shock through the contact surface can either be amplified or attenuated, whereas either a shock wave or a rarefaction wave can be reflected depending on the initial configuration. However, as far as we know, a similar theoretical analysis on the interaction between a shock wave and a rarefaction wave is still not available yet, which may be significant in the future work. The difficulty partly comes from the variation of gas property. In our specific case, before collision the reflected shock wave propagates in the mixture that is compressed by the incident contact surface. After collision, however, the leading shock propagates in a mixture that is compressed by the incident rarefaction wave. Theoretical analysis requires the known of gas thermodynamic conditions in front of and behind the wall-reflected shock wave, incident contact surface, and incident rarefaction wave. It is complex when only the input gas state (i.e., $M_{si,0}$, $p_{si,0}$, and $T_{si,0}$ in Table I) is available.

C. Multi-dimensionality effects

The 1D simulations presented above are computationally efficient, which enable the parametric study on various combustion modes. However, they are unable to account for the multi-dimensionality effects, which generally require at least 2D highly resolved simulations. Non-uniformity behind the reflected shock wave is observed both experimentally^{6,67} and numerically,^{15–17,34,71} which is mainly caused by the interactions between the reflected shock wave and boundary layer developed behind incident shock wave. Furthermore, it is found that under “untailored” conditions, i.e., when the reflected shock interacts with a contact discontinuity, the Richtmyer–Meshkov instability can be induced.^{5,18,72–74} The reflected shock is bifurcated and the uniformity (i.e., one-dimensionality) behind it is violated.⁶ The multi-dimensionality effects on the combustion mode are investigated in this section.

A two-dimensional computational domain is considered. It is 0.1 m in length and 0.025 m in height ($x = 0–100$, $y = 0–25$ mm, see Fig. 13). The 2D domain is discretized with a uniform mesh size of $10 \mu\text{m}$, resulting in a heavy 2D calculations with 25×10^6 cells in total. This resolution is the same as those in the 1D simulations in Secs. IV A and IV B and makes the present case to be a quasi-DNS (Direct Numerical Simulation) study. Such resolution is obviously finer than

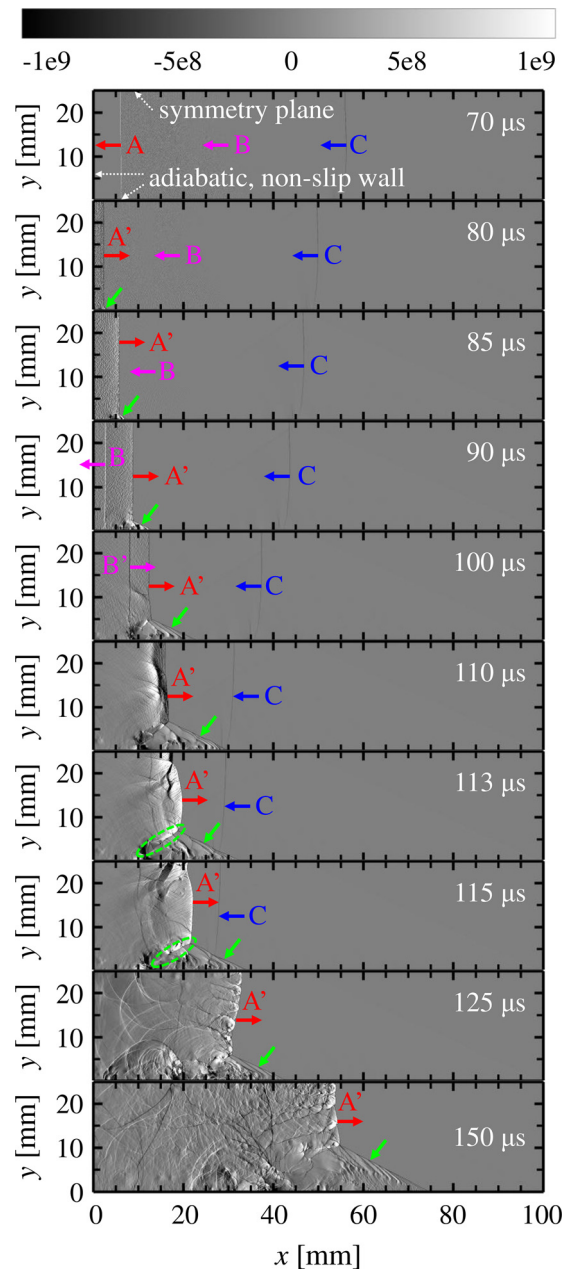


FIG. 13. Evolutions of pressure gradient (in Pa/m). A/A', B/B', and C, respectively, denote the incident/reflected shock waves, incident/reflected compression waves, and incident rarefaction wave. $M_{si,0} = 2.4$ and $\phi_0 = 1.0$, mode 3.

the recent similar 2D simulations of Yamashita *et al.* (25 μm for $\text{C}_2\text{H}_2/\text{O}_2$ mixture),⁶ Kiverin *et al.* (100–200 μm for stoichiometric hydrogen/air mixture),¹⁷ (50, 25, 12.5 μm for $\text{H}_2/\text{O}_2/\text{AR}$ mixture),²⁷ (25 μm for stoichiometric $\text{H}_2/\text{O}_2/\text{AR}$ mixture),⁷¹ and 3D simulations of Lipkowitz *et al.* (100, 50, and 25 μm for stoichiometric H_2/O_2 mixture),¹⁵ (50 μm for H_2/O_2 mixture).¹⁶ It is also comparable to the 2D simulations of Grogan and Ihme (minimum size of 3.125 μm after four levels of adaptive mesh refinement, about 10 cells per C–J detonation induction length for stoichiometric H_2/O_2 mixture).⁷

The left and right boundaries are identical to those in the 1D simulations, whereas the bottom boundary is an adiabatic^{7,75,76} non-slip wall and the top one is symmetric (see Fig. 13). Note that using adiabatic or isothermal wall boundary conditions may cause differences in the combustion mode in some situations,⁷ which however is not the case here. Later, it will be found that the first autoignition hot spot and detonation formation is little affected by the wall. The inflow Mach number is $M_{si,0} = 2.4$ (see Table I), and the initial pressure and temperature of the stoichiometric mixture are also consistent with those in 1D cases, i.e., 10 kPa and 300 K. As a complementary to the 1D simulations in Secs. IV A and IV B, the following discussion is focused on the multi-dimensionality effects. The wave reflections on the wall, various wave interactions, and combustion mode transition discussed in detail in the 1D simulations are not repeated here.

Figure 13 shows the evolutions of pressure gradient to visualize the various wave interactions and their effects on wall boundary layers. At 70 μs , the incident shock wave A is close to the left wall, whereas the contact surface B and rarefaction wave C follow. At 80 μs , the incident shock A is reflected into A'. Meanwhile, a small separation bubble in the boundary layer occurs at the corner between the reflected shock and bottom wall (green arrow). It is induced by the reflected shock and wall boundary layer (developed behind the incident shock wave) interactions.^{6–8,44} At 85 μs , the separation bubble slowly grows before the reflected shock A' collides with contact surface B. Furthermore, at 90 μs , noticeable growth of the bubble is observed after A'/B collision. At 100 μs , B evolves into B' after reflection, and A' is significantly bifurcated by the bubble. The mechanism of the reflected shock wave bifurcation is demonstrated in e.g., Refs. 6, 8, 17, 77, and 78, which is mainly caused by the reflected shock/boundary layer interactions. A λ -shaped flow separation region is formed between the reflected shock and bottom wall. However, above this region, A' is generally planar in the central flow (also termed as the planar part of reflected shock⁶).

At 110 μs , the planar part of A' is also destabilized because of its collision with reflected compression wave B'. Shortly after that, at 113 and 115 μs , the planar part of A' is distorted, i.e., above the λ -shaped region, the shock front moves slower in x -direction, closer to the center plane. Similar observation is also made by Yamashita *et al.*⁶ This is because the flow close to the bottom wall is compressed and hence slightly accelerated by the left bifurcation of the λ -shaped bubble (ellipses). At 125 μs , however, the shock front closer to the central region moves faster. This is because detonation combustion first occurs in the central region, after the collision of the reflected shock A' and incident rarefaction wave C, which will be further confirmed in Fig. 14. It is worth noting that the growth of the separation bubble is suppressed at 110–125 μs , due to the extensive heat release in the central region [see Fig. 14(b)]. At 150 μs , the central section of the reflected shock A' is significantly compressed by the λ -shaped region due to pronounced heat release also occurs in the boundary layer, which hence expands outward and acts as an aerodynamic throat.⁷⁹

Figures 14(a) and 14(b), respectively, show the evolutions of temperature and heat release rate in the foregoing process. At 70 μs , the temperature behind the incident shock A is about 1036.8 K (see Table I), and there is no observable heat release rate. At 80 μs , the mixture temperature is increased to 1774.7 K with obvious heat release rate (e.g., about $5 \times 10^{11} \text{ W/m}^3$) behind the reflected shock A'. At 85 μs , a planar deflagration flame front (with strong heat release rate of about $4 \times 10^{12} \text{ W/m}^3$) is developed above the separation bubble, behind the reflected shock. Therefore, the first autoignition front is purely induced from the reflected shock compression, instead of wave interactions or wall boundary layers. At 90 μs , however, the deflagration flame is significantly weakened (with heat release rate decreased to about 10^{11} W/m^3 behind the shock) because of the reflected shock wave/incident contact surface interactions. On the other hand, wall boundary layers significantly grow after the two-wave collision at 100 μs , which distort and extrude the adjacent shock, hence increase the post-shock gas temperature on the left bifurcation of the λ -shaped region (which is termed as tail shock^{15,16}). Therefore, noticeable heat release rate first recovers around the shock/bubble interfaces [but still lags behind the leading shock, see the ellipse in Fig. 14(b)].

At 110 μs , above the separation bubble a slightly distorted deflagration flame is fully recovered after the collision of the reflected compression wave B'/shock wave A' (see Fig. 13). The flame front is close to the shock front with heat release rate above 10^{12} W/m^3 . At 113 and 115 μs , the DDT process proceeds and temperature right behind the shock front is significantly increased compared with that at 110 μs . However, inside the boundary layers, temperature is pretty low with no obvious heat release, mainly because that the gas is not compressed by the reflected shock like the central flow. At 125 μs , noticeable heat release rate also occurs inside the wall boundary layers, which increases the bubble temperature and expands it outwards. The expansion of the wall boundary layers compresses the planar part of the detonation front, and the height (i.e., y -direction) of the latter is decreased at 150 μs . The left bifurcation of the λ -shaped region (ellipse) is also ignited by the hot burned gas. In addition, there is also increased propensity of autoignition in the right bifurcation of the bubble (arrow, which is also an oblique shock^{15,16}). This is because as the bubble grows, it has increased resistance on the left-flowing gas on its right side and hence the oblique shock gets stronger. This will be further stressed in Fig. 15. Furthermore, no near-wall hot spots ever occur after 90 μs because the mixture there is already burned [see Fig. 14(b)]. However, the near-wall temperature is still increased after 90 μs due to various wave compression.

Figure 15 shows the time sequence of chemical timescale distribution to quantify the mixture reactivity affected by wave interactions and boundary layers. Behind the incident shock $t_e \approx 10^{-3} \text{ s}$, and for the un-shocked gas $t_e \gg 10 \text{ s}$. Behind the reflected shock A', $t_e \approx 10^{-5} \text{ s}$. At 85–90 μs , t_e further drops to about 10^{-6} s behind the reflected shock A' after A'/B collision, because although the deflagration flame is weakened (see Fig. 14), it is not fully quenched. At 110–115 μs , the separation bubble also shows increased reactivity. Note that the smallest t_e lies between the reaction front and leading shock. However, at 125 and 150 μs , the reaction front and leading shock is fully coupled. The distribution of t_e is also significantly affected by the various wave interaction in the post-shock region.

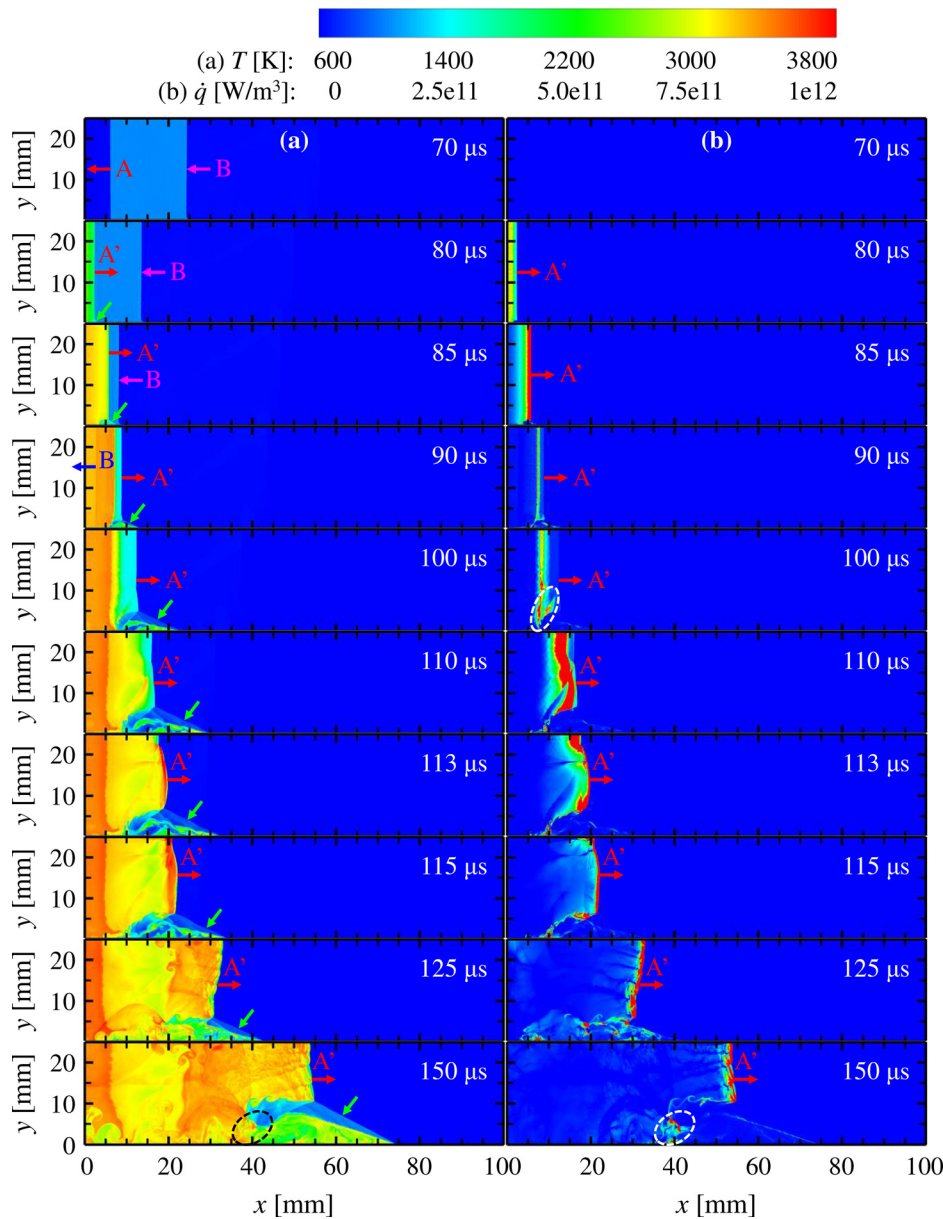


FIG. 14. Evolutions of (a) temperature and (b) heat release rate. Letter symbols same as in Fig. 13.

It should be mentioned that the preceding results may be different for hydrogen/oxygen mixtures in the following two aspects. First, the ignition delay time of H_2/O_2 is generally much shorter than that of C_2H_4/air under the similar thermodynamic conditions. This would extend the upper and lower limits of equivalence ratio for detonation in Fig. 2. Similarly, detonation can occur under lower inflow Mach numbers. Second, the gas properties (e.g., density, heat capacity, and specific heat ratio) of H_2/O_2 system are significantly different from those of C_2H_4/air . This also applies for their final products, i.e., H_2O vs $H_2O + CO_2 + N_2$. These differences may lead to different behaviors of wave interaction as discussed in Figs. 11 and 12. It is worthy to perform similar investigations on the H_2/O_2 mixture in the future, considering the various wave interactions.

V. CONCLUSION

Autoignition and deflagration-to-detonation transition in pre-mixed ethylene/air mixtures behind reflected shock are investigated with highly resolved numerical simulations. Reduced mechanism for ethylene combustion is considered. Different premixture equivalence ratios ($\phi_0 = 0.2 - 2.0$) and incident shock Mach numbers ($M_{si,0} = 1.8 - 3.2$) are studied.

A diagram describing combustion modes of ethylene/air mixture compressed by the shock is first developed. Four modes can be identified, including (1) no ignition, (2) deflagration combustion behind reflected shock, (3) detonation combustion behind reflected shock, and (4) deflagration combustion behind the incident shock (also

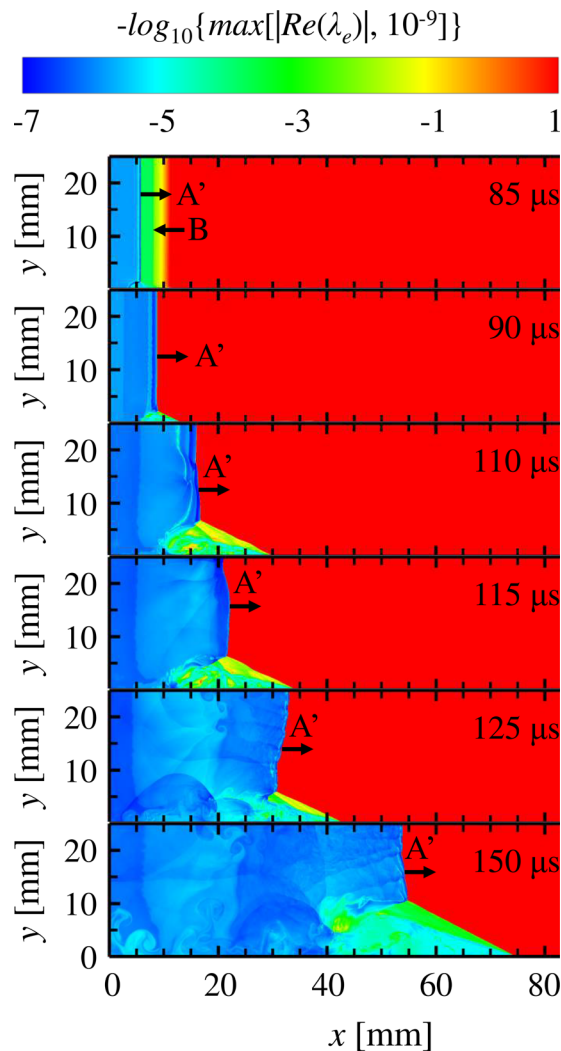


FIG. 15. Evolutions of chemical timescale (in logarithmic scale). Letter symbols same as in Fig. 13.

develops to detonation behind reflected shock). Equivalence ratios and shock Mach numbers strongly affect the combustion development process. Under low $M_{si,0}$ and/or low ϕ_0 , no ignition ($M_{si,0} \leq 1.8$ or $M_{si,0} = 2.0$ but $\phi_0 \leq 0.4$) or deflagration-only mode (two cases with $M_{si,0} = 2.0$ and $\phi_0 = 0.6$, $M_{si,0} = 2.4$ and $\phi_0 = 0.2$) is observed. Mode 3 becomes more prevalent when $M_{si,0}$ and ϕ_0 increases ($\phi_0 \geq 0.8$ and $M_{si,0} = 2.0$, $\phi_0 \geq 0.4$ and $M_{si,0} = 2.4$, $\phi_0 = 0.2-2.0$ and $M_{si,0} = 2.8$). When $M_{si,0} = 3.2$, mode 4 is observed for all the considered equivalence ratios. Moreover, the influence of equivalence ratio on combustion mode is weaker than that of inflow Mach number.

For modes 2 and 3, the gas between the incident shock and contact surface is only in the reaction induction period, whereas for mode 4 a deflagration flame is formed right behind the incident shock. Moreover, three autoignition hot spots are observed in mode 3. The first one occurs at the wall surface, induced from the sequentially re-compression of the reflected shock wave and reflected compression

wave, which further develops to a reaction shock because of “the explosion in the explosion” regime. The second one is induced from the interactions between the reflected shock and incident rarefaction wave. The last one is induced by the intensified reflected shock after interacting with rarefaction wave, in the compressed mixture. It further develops to a reaction wave and couples with the reflected shock after a DDT process, and eventually detonation combustion is formed. However, in mode 2 besides the first hot spot at the wall surface, only one more hot spot is induced off the wall. It is also induced from the reflected shock/rarefaction wave collision, however, with pronounced delay. Furthermore, although it also develops to a reaction wave, it cannot catch up with the reflected shock to support a propagating detonation, before the latter arrives at the right end. For mode 4, deflagration combustion is induced by the incident shock compression whereas detonation occurs after the shock reflection.

The influence of wave interactions on chemical reactions behind the foregoing combustion modes is also interpreted. The chemical timescale from CEMA shows that the mixture reactivity decreases after the reflected shock/contact surface interaction but increases behind the incident and reflected shocks, as well as after the reflected shock/rarefaction wave interaction. Therefore, chemical reactions behind the reflected shock are weakened by contact surface, whereas intensified by rarefaction wave. The time series analysis of primitive variables including pressure, temperature and gas velocity shows that the weakening/strengthening of chemical reactions behind the reflected shock by contact surface/rarefaction wave is mainly caused by the change of pre-shock gas thermodynamic state in the reflected shock frame.

The multi-dimensionality effects are also examined with high-resolution two-dimensional simulations. The reflected shock wave/boundary layer interaction, reflected shock bifurcation, destabilization, and detonation are all observed. Bifurcation and destabilization of the reflected shock first occur in the near wall region because of boundary layer development behind the incident shock wave. Furthermore, destabilization of the central planar part of the reflected shock is intensified by incident contact surface because of the Richtmyer–Meshkov instability mechanism. Planar autoignition is purely induced from reflected shock compression, whereas detonation combustion is formed first in the central region due to the collision of reflected shock and reflected compression wave. The left and right bifurcations of the separation region in the wall boundary layer are then sequentially ignited, respectively, caused by the strengthened compression from the central detonation region and intensified oblique shock.

SUPPLEMENTARY MATERIAL

See the [supplementary material](#) for the sensitivity analysis about mesh resolution and chemical mechanism.

ACKNOWLEDGMENTS

The computational work for this article was performed on resources of ASPIRE 1 Cluster in the National Supercomputing Center, Singapore (<https://www.nscg.sg/>), and Fugaku Cluster in the RIKEN Center for Computational Science in Japan (<https://www.hpci-office.jp/>). This work was funded by MOE Tier 1 Research Grant (No. R-265-000-653-114). Professor Zhuyin Ren and Dr. Wantong Wu from Tsinghua University are thanked for sharing the CEMA routines. Dr. Ruixuan Zhu from the University of Oxford is thanked for the 1D simulations with detailed chemistry.

AUTHOR DECLARATIONS

Conflict of Interest

The authors have no conflicts to disclose.

Author Contributions

Zhiwei Huang: Conceptualization (equal); Formal analysis (equal); Investigation (equal); Methodology (equal); Validation (equal); Visualization (equal); Writing – original draft (equal). **Huangwei Zhang:** Conceptualization (equal); Funding acquisition (equal); Investigation (equal); Project administration (equal); Resources (equal); Software (equal); Supervision (equal); Writing – review and editing (equal).

DATA AVAILABILITY

The data that support the findings of this study are available from the corresponding author upon reasonable request.

REFERENCES

- A. Jach, W. Rudy, A. Pękalski, and A. Teodorczyk, "Assessment of detailed reaction mechanisms for reproduction of ignition delay times of C2–C6 alkenes and acetylene," *Combust. Flame* **206**, 37–50 (2019).
- A. Chauvin, G. Jourdan, E. Daniel, L. Houas, and R. Tosello, "Experimental investigation of the propagation of a planar shock wave through a two-phase gas–liquid medium," *Phys. Fluids* **23**, 113301 (2011).
- G. J. Sharpe, "Shock-induced ignition for a two-step chain-branching kinetics model," *Phys. Fluids* **14**, 4372–4388 (2002).
- S. Udagawa, K. Maeno, I. Golubeva, and W. Garen, "Interferometric signal measurement of shock waves and contact surfaces in small scale shock tube," in *Shock Waves* (Springer, 2009), pp. 1419–1424.
- J. T. Peace and F. K. Lu, "Detonation-to-shock wave transmission at a contact discontinuity," *Shock Waves* **28**, 981–992 (2018).
- H. Yamashita, J. Kasahara, Y. Sugiyama, and A. Matsuo, "Visualization study of ignition modes behind bifurcated-reflected shock waves," *Combust. Flame* **159**, 2954–2966 (2012).
- K. P. Grogan and M. Ihme, "Weak and strong ignition of hydrogen/oxygen mixtures in shock-tube systems," *Proc. Combust. Inst.* **35**, 2181–2189 (2015).
- K. P. Grogan and M. Ihme, "Regimes describing shock boundary layer interaction and ignition in shock tubes," *Proc. Combust. Inst.* **36**, 2927–2935 (2017).
- O. G. Penyazkov, K. L. Sevrouk, V. Tangirala, and N. Joshi, "High-pressure ethylene oxidation behind reflected shock waves," *Proc. Combust. Inst.* **32**, 2421–2428 (2009).
- S. Saxena, M. S. P. Kahandawala, and S. S. Sidhu, "A shock tube study of ignition delay in the combustion of ethylene," *Combust. Flame* **158**, 1019–1031 (2011).
- Z. Wan, Z. Zheng, Y. Wang, D. Zhang, P. Li, and C. Zhang, "A shock tube study of ethylene/air ignition characteristics over a wide temperature range," *Combust. Sci. Technol.* **192**, 2297–2305 (2020).
- O. Trass and D. Mackay, "Contact surface tailoring in a chemical shock tube," *AIAA J.* **1**, 2161–2163 (1963).
- C. Huang, C. Qi, and Z. Chen, "Non-uniform ignition behind a reflected shock and its influence on ignition delay measured in a shock tube," *Shock Waves* **29**, 957–967 (2019).
- J. Melguizo-Gavilanes and L. Bauwens, "A comparison between constant volume induction times and results from spatially resolved simulation of ignition behind reflected shocks: implications for shock tube experiments," *Shock Waves* **23**, 221–231 (2013).
- J. T. Lipkowitz, I. Wlokas, and A. M. Kempf, "Analysis of mild ignition in a shock tube using a highly resolved 3D-LES and high-order shock-capturing schemes," *Shock Waves* **29**, 511–521 (2019).
- J. T. Lipkowitz, D. Nativel, S. Cooper, I. Wlokas, M. Fikri, E. Petersen, C. Schulz, and A. M. Kempf, "Numerical investigation of remote ignition in shock tubes," *Flow, Turbul. Combust.* **106**, 471–498 (2021).
- A. D. Kiverin, K. O. Minaev, and I. S. Yakovenko, "Modes of mild ignition in shock tubes: Origins and classification," *Combust. Flame* **221**, 420–428 (2020).
- F. Cobos-Campos and J. G. Wouchuk, "Analytic solution for the zero-order postshock profiles when an incident planar shock hits a planar contact surface," *Phys. Rev. E* **100**, 033107 (2019).
- D. Bitondo, I. I. Glass, and G. N. Patterson, "One dimensional theory of absorption and amplification of a plane shock wave by a gaseous layer," University of Toronto Institute of Aerophysics Report. No. 7, 1950.
- S. G. Saytzev and R. I. Soloukhin, "Study of combustion of an adiabatically-heated gas mixture," *Symp. Combust.* **8**, 344–347 (1961).
- B. L. Wang, H. Olivier, and H. Grönig, "Ignition of shock-heated H₂–air–steam mixtures," *Combust. Flame* **133**, 93–106 (2003).
- V. V. Voevodsky and E. I. Soloukhin, "On the mechanism and explosion limits of hydrogen–oxygen chain self-ignition in shock waves," *Symp. Combust.* **10**, 279–283 (1965).
- J. W. Meyer and A. K. Oppenheim, "On the shock-induced ignition of explosive gases," *Symp. Combust.* **13**, 1153–1164 (1971).
- Y. Takano, "Numerical simulations for shock-tube experiments of reflected-shock waves in combustible gas," *JSME Int. J., Ser. B.* **36**, 300–306 (1993).
- E. Dziemińska and A. K. Hayashi, "Auto-ignition and DDT driven by shock wave-boundary layer interaction in oxyhydrogen mixture," *Int. J. Hydrogen Energy* **38**, 4185–4193 (2013).
- E. Ninnemann, B. Koroglu, O. Pryor, S. Barak, L. Nash, Z. Loparo, J. Sosa, K. Ahmed, and S. Vasu, "New insights into the shock tube ignition of H₂/O₂ at low to moderate temperatures using high-speed end-wall imaging," *Combust. Flame* **187**, 11–21 (2018).
- A. D. Kiverin and I. S. Yakovenko, "Evolution of wave patterns and temperature field in shock-tube flow," *Phys. Rev. Fluids* **3**, 053201 (2018).
- O. Pryor, S. Barak, B. Koroglu, E. Ninnemann, and S. S. Vasu, "Measurements and interpretation of shock tube ignition delay times in highly CO₂ diluted mixtures using multiple diagnostics," *Combust. Flame* **180**, 63–76 (2017).
- M. Figueroa-Labastida and A. Farooq, "Simultaneous lateral and endwall high-speed visualization of ignition in a circular shock tube," *Combust. Flame* **214**, 263–265 (2020).
- V. V. Martynenko, O. G. Penyaz'kov, K. A. Ragothner, and S. I. Shabunya, "High-temperature ignition of hydrogen and air at high pressures downstream of the reflected shock wave," *J. Eng. Phys. Thermophys.* **77**, 785–793 (2004).
- R. Blumenthal, K. Fieweger, K. H. Komp, and G. Adomeit, "Gas dynamic features of self ignition of non diluted fuel/air mixtures at high pressure," *Combust. Sci. Technol.* **113**, 137–166 (1996).
- G. Thomas, "Some observations on the initiation and onset of detonation," *Philos. Trans. R. Soc. A* **370**, 715–739 (2012).
- Y. Onishi, "On flows behind shock waves reflected from a solid wall," *Shock Waves* **1**, 293–299 (1991).
- E. S. Oran and V. N. Gamezo, "Origins of the deflagration-to-detonation transition in gas-phase combustion," *Combust. Flame* **148**, 4–47 (2007).
- D. J. Singh and C. J. Jachimowski, "Quasiglobal reaction model for ethylene combustion," *AIAA J.* **32**, 213–216 (1994).
- G. L. Pellett, S. N. Vaden, and L. G. Wilson, "Gaseous surrogate hydrocarbons for a HiFIRE scramjet that mimic opposed jet extinction limits for cracked JP fuels," in *55th JANNAF Propulsion Meeting* (NASA, 2008), pp. 12–16, <https://ntrs.nasa.gov/citations/20080020388>.
- G. J. Sharpe and M. Short, "Ignition of thermally sensitive explosives between a contact surface and a shock," *Phys. Fluids* **19**, 126102 (2007).
- S. H. Lam and D. A. Goussis, "The CSP method for simplifying kinetics," *Int. J. Chem. Kinet.* **26**, 461–486 (1994).
- T. F. Lu, C. S. Yoo, J. H. Chen, and C. K. Law, "Three-dimensional direct numerical simulation of a turbulent lifted hydrogen jet flame in heated coflow: A chemical explosive mode analysis," *J. Fluid Mech.* **652**, 45–64 (2010).
- W. Wu, Y. Piao, Q. Xie, and Z. Ren, "Flame diagnostics with a conservative representation of chemical explosive mode analysis," *AIAA J.* **57**, 1355–1363 (2019).
- D. A. Goussis, H. G. Im, H. N. Najm, S. Paolucci, and M. Valorani, "The origin of CEMA and its relation to CSP," *Combust. Flame* **227**, 396–401 (2021).
- Z. Luo, C. S. Yoo, E. S. Richardson, J. H. Chen, C. K. Law, and T. Lu, "Chemical explosive mode analysis for a turbulent lifted ethylene jet flame in highly-heated coflow," *Combust. Flame* **159**, 265–274 (2012).

- ⁴³Z. Huang, M. Zhao, Y. Xu, G. Li, and H. Zhang, "Eulerian–Lagrangian modeling of detonative combustion in two-phase gas–droplet mixtures with OpenFOAM: Validations and verifications," *Fuel* **286**, 119402 (2021).
- ⁴⁴Y. Uygun, S. Ishihara, and H. Olivier, "A high pressure ignition delay time study of 2-methylfuran and tetrahydrofuran in shock tubes," *Combust. Flame* **161**, 2519–2530 (2014).
- ⁴⁵See <https://Blog.Nus.Edu.Sg/Huangwei/Nus-Ryrhocentralfoam-Solver/> for more information about the development and validation of the RYrhoCentralFoam solver.
- ⁴⁶H. Zhang, M. Zhao, and Z. Huang, "Large eddy simulation of turbulent supersonic hydrogen flames with OpenFOAM," *Fuel* **282**, 118812 (2020).
- ⁴⁷C. J. Greenshields, H. G. Weller, L. Gasparini, and J. M. Reese, "Implementation of semi-discrete, non-staggered central schemes in a collocated, polyhedral, finite volume framework, for high-speed viscous flows," *Int. J. Numer. Methods Fluids* **63**, 1–21 (2010).
- ⁴⁸Z. Huang, M. Zhao, and H. Zhang, "Modelling *n*-heptane dilute spray flames in a model supersonic combustor fueled by hydrogen," *Fuel* **264**, 116809 (2020).
- ⁴⁹J. Crank and P. Nicolson, "A practical method for numerical evaluation of solutions of partial differential equations of the heat-conduction type," *Math. Proc. Cambridge Philos. Soc.* **43**, 50–67 (1947).
- ⁵⁰A. Kurganov, S. Noelle, and G. Petrova, "Semidiscrete central-upwind schemes for hyperbolic conservation laws and Hamilton–Jacobi equations," *SIAM J. Sci. Comput.* **23**, 707–740 (2001).
- ⁵¹A. Kurganov and E. Tadmor, "New high-resolution central schemes for nonlinear conservation laws and convection-diffusion equations," *J. Comput. Phys.* **160**, 241–282 (2000).
- ⁵²P. Roe, "Characteristic-based schemes for the Euler equations," *Annu. Rev. Fluid Mech.* **18**, 337–365 (1986).
- ⁵³H. Jasak, "Error analysis and estimation for the finite volume method with applications to fluid flows," Ph.D. thesis (Imperial College, London, 1996).
- ⁵⁴E. Hairer and G. Wanner, *Solving Ordinary Differential Equations II: Stiff and Differential-Algebraic Problems*, 2nd ed. (Springer, 1996), p. 14.
- ⁵⁵B. McBride, S. Gordon, and M. Reno, "Coefficients for calculating thermodynamic and transport properties of individual species," NASA Technical Memorandum No. 4513, 1993.
- ⁵⁶C. J. Jachimowski, "An experimental and analytical study of acetylene and ethylene oxidation behind shock waves," *Combust. Flame* **29**, 55–66 (1977).
- ⁵⁷L. Zhang, J. Y. Choi, and V. Yang, "Supersonic combustion and flame stabilization of coflow ethylene and air with splitter plate," *J. Propul. Power* **31**, 1242–1255 (2015).
- ⁵⁸B. Liu, G. He, F. Qin, Q. Lei, J. An, and Z. Huang, "Flame stabilization of supersonic ethylene jet in fuel-rich hot coflow," *Combust. Flame* **204**, 142–151 (2019).
- ⁵⁹J. Fujii, Y. Kumazawa, A. Matsuo, S. Nakagami, K. Matsuoka, and J. Kasahara, "Numerical investigation on detonation velocity in rotating detonation engine chamber," *Proc. Combust. Inst.* **36**, 2665–2672 (2017).
- ⁶⁰H. Watanabe, A. Matsuo, K. Matsuoka, A. Kawasaki, and J. Kasahara, "Numerical investigation on propagation behavior of gaseous detonation in water spray," *Proc. Combust. Inst.* **37**, 3617–3626 (2019).
- ⁶¹H. Wang and A. Laskin, "A comprehensive kinetic model of ethylene and acetylene oxidation at high temperatures," Progress Report, 1999, <http://ignis.usc.edu/Mechanisms/C2-C4/c2.pdf>.
- ⁶²M. Zhao, Z. Ren, and H. Zhang, "Pulsating detonative combustion in *n*-heptane/air mixtures under off-stoichiometric conditions," *Combust. Flame* **226**, 285–301 (2021).
- ⁶³W. Han, C. Wang, and C. K. Law, "Pulsation in one-dimensional H₂–O₂ detonation with detailed reaction mechanism," *Combust. Flame* **200**, 242–261 (2019).
- ⁶⁴N. M. Rubtsov, *The Modes of Gaseous Combustion*, 1st ed. (Springer, 2016).
- ⁶⁵A. C. Merkel and G. Ciccarelli, "Visualization of lean methane–air ignition behind a reflected shock wave," *Fuel* **271**, 117617 (2020).
- ⁶⁶T. Jaravel, O. Dounia, Q. Malé, and O. Vermorel, "Deflagration to detonation transition in fast flames and tracking with chemical explosive mode analysis," *Proc. Combust. Inst.* **38**, 3529–3536 (2021).
- ⁶⁷D. H. Edwards, G. O. Thomas, and T. L. Williams, "Initiation of detonation by steady planar incident shock waves," *Combust. Flame* **43**, 187–198 (1981).
- ⁶⁸H. R. Yu, B. Esser, M. Lenartz, and H. Grönig, "Gaseous detonation driver for a shock tunnel," *Shock Waves* **2**, 245–254 (1992).
- ⁶⁹F. K. Lu, D. R. Wilson, R. J. Bakos, and J. I. Erdos, "Recent advances in detonation techniques for high-enthalpy facilities," *AIAA J.* **38**, 1676–1684 (2000).
- ⁷⁰A. Saso, *Compressible Fluid Dynamics and Shock Waves*, 1st ed. (Springer, 2020).
- ⁷¹A. D. Kiverin and I. S. Yakovenko, "Ignition and detonation onset behind incident shock wave in the shock tube," *Combust. Flame* **204**, 227–236 (2019).
- ⁷²M. Brouillette, "The Richtmyer–Meshkov instability," *Annu. Rev. Fluid Mech.* **34**, 445–468 (2002).
- ⁷³F. C. Campos and J. G. Wouchuk, "Analytical scalings of the linear Richtmyer–Meshkov instability when a shock is reflected," *Phys. Rev. E* **93**, 053111 (2016).
- ⁷⁴F. Cobos Campos and J. G. Wouchuk, "Analytical asymptotic velocities in linear Richtmyer–Meshkov-like flows," *Phys. Rev. E* **90**, 053007 (2014).
- ⁷⁵Y. S. Weber, E. S. Oran, J. P. Boris, and J. D. Anderson, "The numerical simulation of shock bifurcation near the end wall of a shock tube," *Phys. Fluids* **7**, 2475–2488 (1995).
- ⁷⁶A. Khokhlov, J. Austin, C. Bacon, S. Aithal, and K. Riley, "Reflected shock bifurcation in a square channel," AIAA Paper No. 2011-646, 2011.
- ⁷⁷H. Kleine, V. N. Lyakhov, L. G. Gvozdeva, and H. Grönig, "Bifurcation of a reflected shock wave in a shock tube," in *Shock Waves* (Springer, 1992), pp. 261–266.
- ⁷⁸O. Penyazkov and A. Skilandz, "Bifurcation parameters of a reflected shock wave in cylindrical channels of different roughnesses," *Shock Waves* **28**, 299–309 (2018).
- ⁷⁹Z. Huang and H. Zhang, "Numerical investigations of mixed supersonic and subsonic combustion modes in a model combustor," *Int. J. Hydrogen Energy* **45**, 1045–1060 (2020).